STUDYING THE OXYGEN EFFECT IN PROTON THERAPY VIA GPU-BASED MICROSCOPIC MONTE CARLO SIMULATION

by

MARCOS JOSEPH GUILLEN

THESIS

Submitted in partial fulfillment of the requirements

for the degree of Master of Science in Physics at

The University of Texas at Arlington

August 2020

Arlington, Texas

Supervising Committee:

Dr. Yujie Chi, Supervising Professor

Dr. Mingwu Jin

Dr. Wei Chen

Dr. Amir Shahmoradi

Dedicated to:

Nuria J. Huesca

ACKNOWLEDGMENTS

First and foremost, I would like to thank my research advisor Dr. Yujie Chi. I would also like to thank Dr. Ramon Lopez. Thank you for giving me this chance to further my educational career. It has been such a wonderful time here at UTA and would not have been possible without your help and guidance as well. I would also like to thank the wonderful faculty staff at the physics department. Thank you for making me feel welcomed and creating such a wonderful learning and work environment. Special thanks to my research group Damon, Harsh, Youfang, and Dr. Chalise. You guys are the best group I could ask for, you guys made research a fun and enjoyable experience. I would also like to thank Dr. Chen and his research group for expanding my knowledge on nanoparticles and cell studies. I would also like to thank all my fellow peers in the physics department. I would also like to thank all other committee members for my thesis defense, Dr. Jin and Dr. Shahmoradi. Thank you for your time and guidance. I would like to thank my family for helping me get through graduate school. It has not been easy, but you helped me get through it. Last but not least I would like to thank my mother Nuria J. Huesca without whose help none of this would have been possible.

August 7, 2020

ABSTRACT

STUDYING THE OXYGEN EFFECT IN PROTON THERAPY VIA GPU-BASED MICROSCOPIC MONTE CARLO SIMULATION

Marcos Joseph Guillen, MS

The University of Texas at Arlington, 2020

Dissolved oxygen molecules are known to play an important role in radiotherapy. For example, tumor cells can be more radio-resistance under hypoxia than normoxia. There has been multiple hypothesis proposed to explain these phenomena, including the oxygen mediated chemical track evolution. In principle, we can perform microscopic Monte Carlo (MC) simulation to quantitively test this hypothesis. Yet, to avoid the extreme high computational resource consuming, in the current CPU-based MC tools, oxygen is either ignored or taken as a continuous radical-scavenging background. Recently, our research group developed an open-source, GPU-based MC simulation tool, gMicroMC, in which, the oxygen mediated chemical track evolution was modeled in a step-by-step manner. In this project, we applied gMicroMC to study the radical evolution under different oxygen levels for proton induced water radiolysis. Compared to the continuous background method, the oxygen was found consumed slower with gMicroMC. We also documented the errors and issues as a fresh user of gMicroMC. A further automation for some parameter settings can make it more user-friendly.

Marcos Joseph Guillen, MS

The University of Texas at Arlington, 2020

Table of Contents

Contents

LIST OF FIGURES

CHAPTER 1: INTRODUCTION

1.1 Ionizing radiation (IR) and its microscopic overview

Ionizing radiation (IR), including energetic x-rays, gamma-rays, electrons, protons and other ions, imparts its energy to the medium mainly through ionization. Shortly after the discovery of x-ray, the first type of IR, in 1895 by Roentgen, it was quickly adopted in clinic in the format of medical diagnostic imaging, which still plays an important role even in our current clinic (1, 2). Yet two years later, the rays' dangerous side began to be reported: examples included loss of hair and skin burns of varying severity. This was correlated to the damaging properties of x-rays on organic systems (3). With this property, x-rays and other IRs then found their application in multiple area, greatly impacting the human society (4). For instance, it has been approved by the FDA for food irradiation in the United States, which can improve the safety and extend the shelf life of foods by reducing or eliminating microorganisms and insects. It has been used in modern medicine in the form of radiosurgery and radiotherapy. With radiosurgery, preselected tissue areas can be precisely destructed while radiotherapy plays an important role in the cancer treatment. More than half of cancer patients receive radiotherapy. The strong damaging effect of IR has also been utilized for nuclear weapon development in military (5).

As for the radiotherapy, it can be generally divided into two types: external-beam radiotherapy (EBRT), using long source–surface–distance (SSD), and brachytherapy, based on a short SSD, initially delivered with radium and later with 50 kV X-rays, and other radioactive source types. No matter which type used, the purpose of radiotherapy is to kill the tumor cells with sufficient radiation deposition while sparing normal tissues as much as possible, since the

damaging of normal tissues could affect their functions, causing radiation-induced side effects. This energy deposition was quantified as radiation dose, which is defined as the ratio between the energy deposited by the IR in a finite volume and the volume mass.

The dose deposition profiles along the IR track were found varied among different IR types (Figure 1). As shown in Figure 1, x-ray has quite different behaviors than proton and carbon ion beams for the depth dose profiles in a water phantom. X-ray is known as a charge neutral particle, while its energy deposition is mainly determined by the secondary electrons produced during its interaction with the phantom material. Proton and carbon ions are all charged particles. Their energy depositions are then governed by the Bethe-Bloch formula (6), in which the energy loss of the incident particle is inversely dependent on its velocity, forming the sharp Bragg peak region.

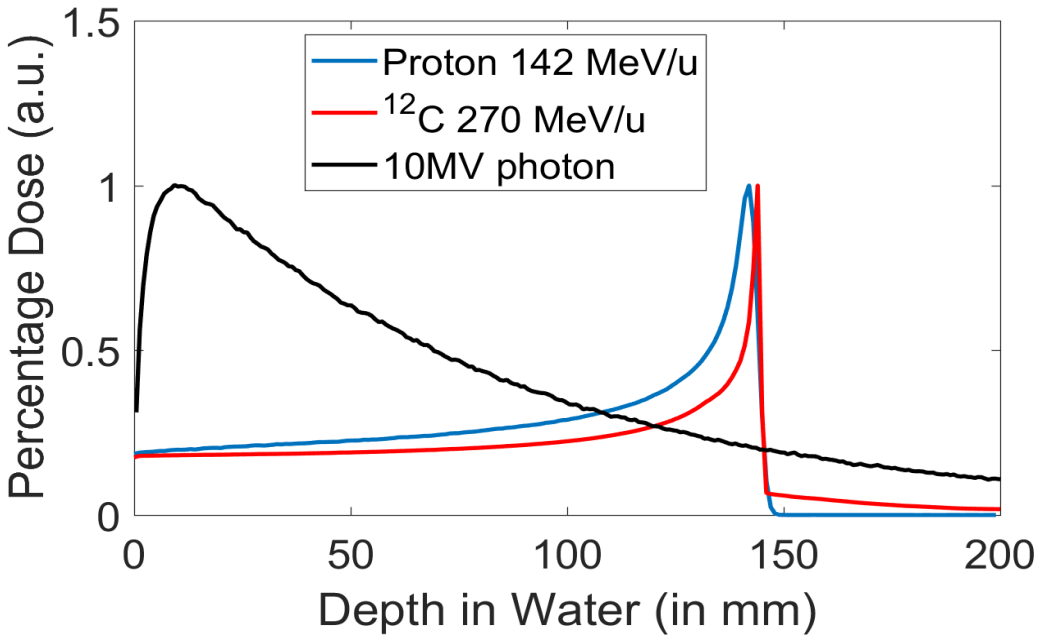

Figure 1.1 The depth dose profiles in water phantom from different IR species: photon (black line), proton (blue line) and carbon ion (red line). The results were obtained from Geant4 simulation.

Due to the existence of these differences in the depth dose profile, the treatment planning, resulted

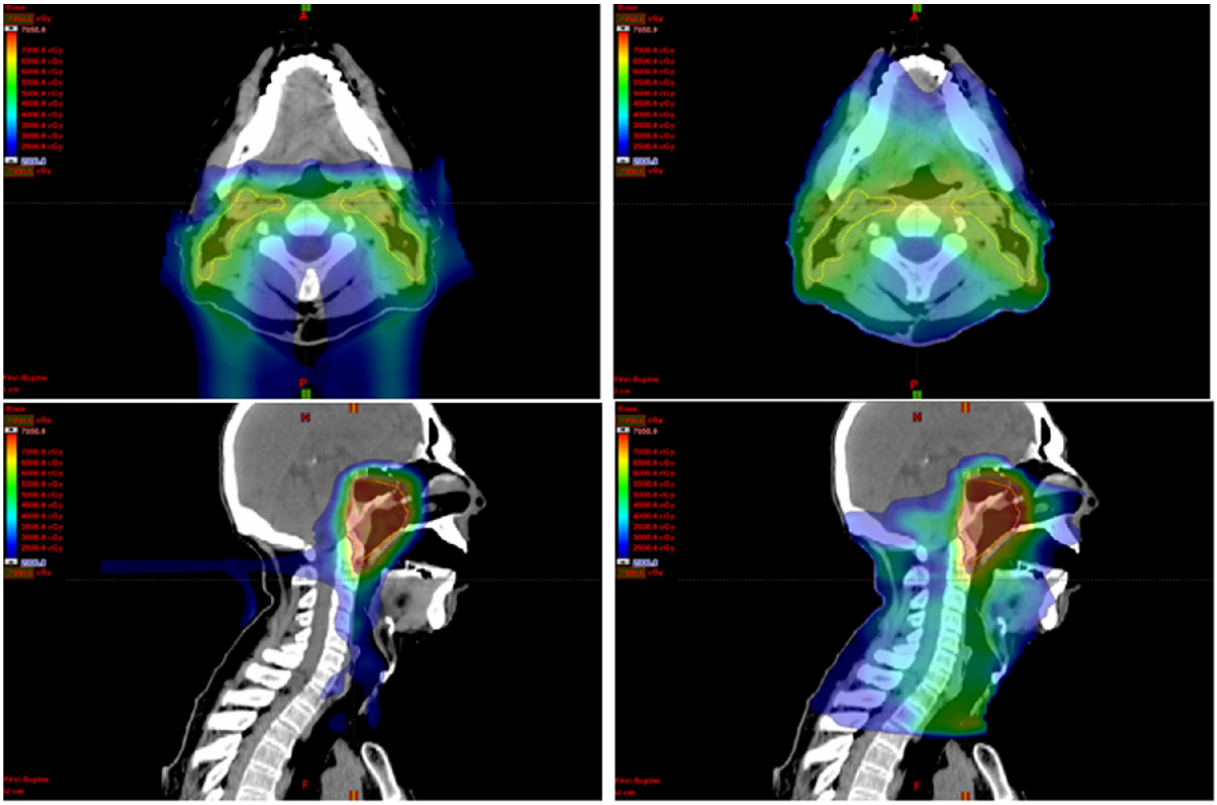

Figure 1.2 Differences in isodose distributions between intensity-modulated proton therapy (IMPT) and intensity-modulated radiotherapy (IMRT). This figure shows the isodose distributions for IMPT (left) and IMRT (right) plans on representative axial, sagittal, and coronal images from the planning CT scan from a patient with nasopharyngeal carcinoma. (7)

dose coverage (Figure 2) and the treatment delivery then can be quite different among different IR species and corresponding modalities.

Further study indicated that the biological damaging effect of IR can also be IR type dependent, which is quantified as relative biological effectiveness (RBE), that is the ratio of a dose of standard radiation to the dose of test radiation to produce the same biological effects. Take the 250 kVp x-ray as the standard radiation and the colonic cell survival rate after radiation as the considered biological effect, the RBE for alpha particle can be as high as 20, that for proton is >1, and that for neutron can be ~100 (8). Even for the same IR type, RBE can be IR energy dependent. Hence, in modern radiotherapy clinic, radiobiological dose distribution is another important factor playing

an important role, except for the physical dose distribution.

Furthermore, the biological damaging effect is also radiation scenarios, such as low or high dose rates, normoxia or hypoxia, etc., dependent (9, 10). Specifically, radiation delivered at extreme high dose rate can be more sparing to normal tissues, while similar effect on tumor killing effect when compared with radiation delivered at conventional dose rate, which is known as the FLASH therapy effect (11). Cancer cells irradiated at hypoxia can be more radio-resistance than those irradiated at normoxia (12), which is quantified as the oxygen enhancement ratio (OER). The definition of OER is that the enhancement of therapeutic or detrimental effect of ionizing radiation due to the presence of oxygen. This so-called oxygen effect is most notable when cells are exposed to an ionizing radiation dose. The value of the maximum OER varies from about 1–4. The maximum OER ranges from about 2-4 for low-LET radiations such as X-rays, beta particles and gamma rays, whereas the OER is unity for high-LET radiations such as low energy alpha particles (13, 14). The IR type dependence of OER indicates a rich physical-biological process behind radiotherapy. More importantly, the oxygen level in normal tissues can be typically higher than that within the tumor cell region. This is because that as a tumor grows, it rapidly outgrows its blood supply, leaving portions of the tumor with regions where the oxygen concentration is significantly lower than in healthy tissues, forming the tumor hypoxia.

Overall, the radiobiological effect of IR is complex. Advanced cellular radiobiological study exhibited that the damage of deoxyribonucleic acid (DNA) plays a pivotal role towards the determination of the final biological/clinical outcomes after IR exposure (15). DNA contains all the code (gene) for the synthesis of proteins, cell reproduction and organization of the tissues and organs, which exists in all populations (16-19). It is hypothesized that when IR interacts with DNA,

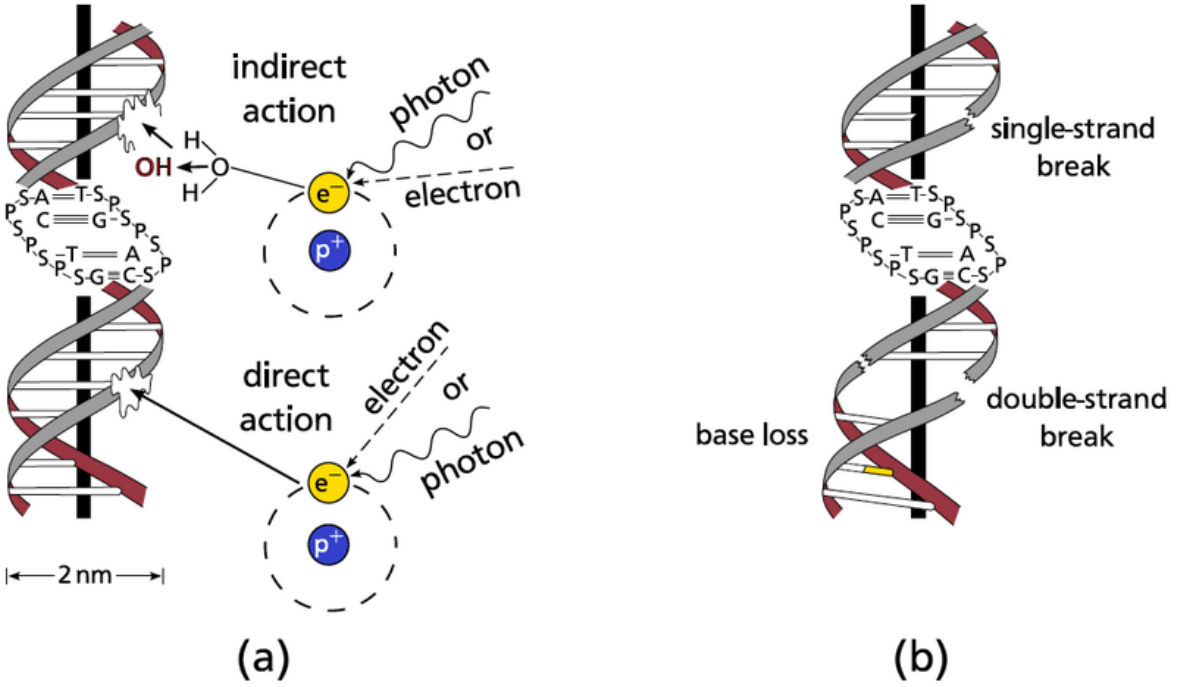

Figure 1.2 (a) Direct and indirect radiation damage to the DNA. Direct damage is caused by energy deposition in direct hits from electrons liberated in ionization processes. Free hydroxyl radicals (OH), formed by ionization in the hydrolysis of water, can cause indirect damage to the DNA in chemical reactions. (b) Schematic illustration of selected types of radiation damage to the DNA (20).

it could damage the DNA microstructures as shown in Figure 3. This includes the direct (physical) damage formed in femto- to pico- seconds by the primary and secondary IR particles in the so-called physical stage, and the indirect (chemical) damage generated in pico- to micro- seconds by subsequently generated radiation radicals in the chemical stage (Figure 3) (5).

Although much knowledge has been accumulated to understand the radiation induced DNA damage at the microscopic level, there are still a lot more to specify. For example, for the OER effect, multiple hypothesis was proposed, yet, none of them has been verified either through experiment or simulation. Hence, it is highly desired that the OER effect can be further studied such that its effect in radiotherapy can be sufficiently optimized.

1.2 Hypothesis of oxygen effect in IR

As mentioned in section 1.1, oxygen is of vital importance in radiotherapy response. This effect has been studied since the 1950's. It has been shown that tumors with better oxygenation respond better to radiotherapy then those with extensive hypoxia which is low levels of oxygen. The presence of molecular oxygen significantly modifies the effectiveness of radiotherapy; relative to anoxia, well oxygenated tumors respond better by a factor of 2.5–3. This boosting fraction is referred as OER (21).

At the molecule level, there are multiple hypothesis proposed to explain the OER effect, including the oxygen reaction effect, oxygen fixation, oxygen in track, etc. (22).

As for the oxygen reaction effect, in oxygenated media, the radiolytic species produced during the physicochemical stage can interact with the molecular oxygen dissolved in the target and lead to an enhanced production of highly toxic reactive oxygen species (ROS). For example, solvated electrons and hydrogen atoms, are generated in large quantities and react with oxygen to form the superoxide anion and its protonated form, which are particularly damaging.

$$e_{aq}^{-} + O_2 \rightarrow O_2^{\cdot -},$$

$$H^{\cdot} + O_2 \rightarrow HO_2^{\cdot}.$$

These products are involved in the lipid peroxidation chain and play an important role in the production of other toxic species, such as hydroxyl radicals $OH^{\cdot}$ through the Haber-Weiss reaction (catalyzed by the presence of transition metals), peroxynitrite ions $ONOO^{\cdot}$ through the interaction with nitrogen monoxide $NO^{\cdot}$, and H_2O_2 after scavenging by superoxide dismutase enzymes (SOD).

As for the oxygen fixation hypothesis (OFH), it states that most DNA can be repaired after radical damage, but that repair is more difficult or impossible when caused by the product of a

radical and an oxygen molecule. When an incoming high energy photon interacts with biological matter, it can cause damage in several ways. It can directly interact with DNA, causing an ionization event. More commonly, it can interact with other organic matter such as water, producing high energy electrons. These ionizing electrons react with water to create highly reactive hydroxyl radicals (R•) which in turn cause DNA base damage. In general, this kind of radical damage is readily chemically repaired. However, when these radicals encounter molecular oxygen, they form a peroxyl radical, $RO_2^{\cdot}$. This is much more damaging, difficult or impossible for the cell to repair. This type of damage can be repaired under hypoxia but when this is (fixed) with high levels of oxygen present. Figure 4 shows what happens under these conditions. We can see that

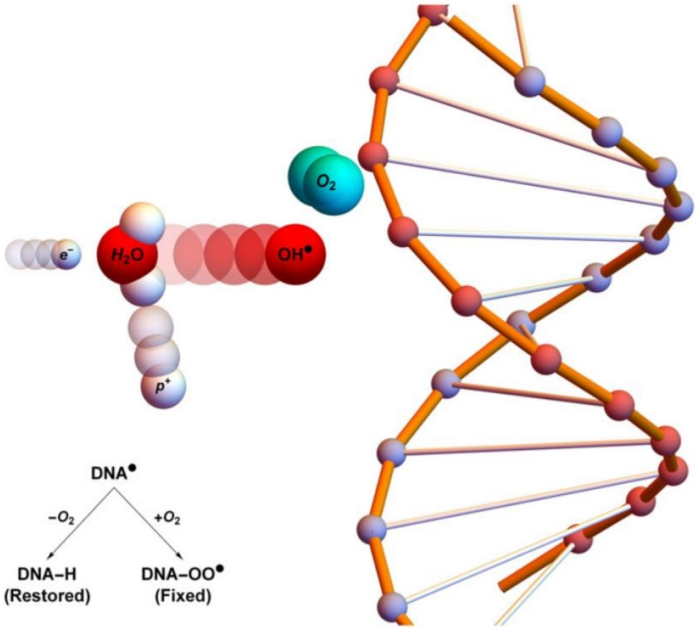

Figure 1.4 Oxygen fixation hypothesis—a high energy electron created by an x-ray photon (e-) impinges upon a water molecule, liberating a proton (p+) and creating a hydroxyl radical (OH•). This reactive molecule then impacts upon DNA, resulting in ionization damage, DNA •. This can be readily repaired to its original state (DNA-H), but in the presence of molecular oxygen a peroxyl radical is formed (DNA-OO •), 'fixing' damage into a permanent irreparable state. (21)

without a molecular oxygen, hydroxyl radical (OH•) impacts upon DNA, resulting in ionization damage, DNA •. This can be readily repaired to its original state (DNA-H). Yet in the presence of molecular oxygen, a peroxyl radical is formed (DNA-OO •), 'fixing' damage into a permanent irreparable state.

1.3 The role of chemical radicals in radiation induced DNA damage

Although multiple hypothesis has been proposed to explain the OER effect in radiotherapy, it lacks quantitative measurement experimentally or via detailed simulation. It has been reported that for the oxygen enhancement effect to be observed, molecular oxygen must be present before irradiation or within microseconds of exposure. No increase in OER occurs if oxygen is added beyond this threshold. It is hence important to tackle the chemical radical generation, diffusion and its DNA damage process in detail.

As stated in section 1.1 and Figure 3, once IR enters into the cell, it could interact with water molecules inside it through ionization and excitation. Immediately after that, the water molecules can be quite unstable, be dissociated, relaxed or auto-ionized, forming the initial distribution of the chemical radicals. Specifically, the possible initial chemical species directly from water molecule cam be $H^+, OH^{-1}, e_{aq}^-, H^{\cdot},$ and $OH^{\cdot}$. These radicals will then diffuse inside the solvent via Brownian motion. During the diffusion process, there is also a possibility that mutual interactions among radicals can happen, which stimulates the chemical species transferring from one type to another, or make both radicals disappear. At the same time, these chemical species can also interact with other dissolved molecules in the solvent or other chemical species, for example, oxygen molecule, radicals forming a specific PH value, or DNA molecules, etc. Consequently, DNA damage can be formed.

Actually, even without radiation, there are toxic chemical species background inside the tumor cells, especially in the format of reactive oxygen species (ROS). The term ROS covers several molecules derived from oxygen that have accepted extra electrons and can oxidize other molecules (23). Most intracellular ROS are derived from the single electron reduction of oxygen (O_2) to form the radical superoxide ($O_2^{\cdot -}$). Two superoxide molecules can then be converted to one molecule of the non-radical ROS molecule hydrogen peroxide (H_2O_2) and one water molecule by superoxide dismutase. Hydrogen peroxide can also accept another electron from free Fe^{2+} by the Fenton reaction to become a hydroxyl radical ($HO^{\cdot}$).

Within the cancerous cell, multiple characteristics can increase the ROS generation, for example, the oncogenes, the mitochondrial mutations, hypoxia and tumor suppressor loss, etc. Due to these processes, the ROS level can be increased much higher than that in the cytostatic (normal)

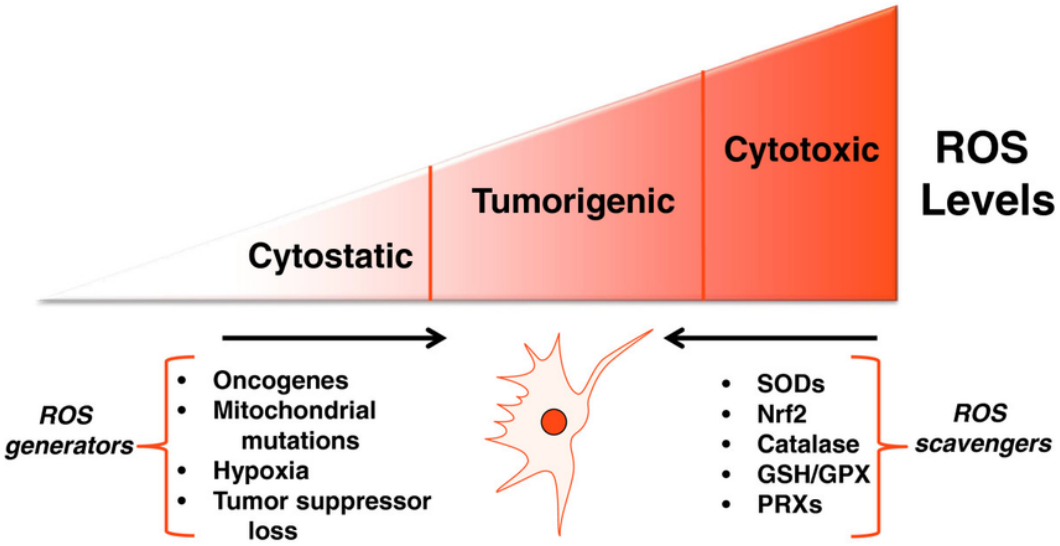

Figure 1.5 Balancing ROS generation and ROS scavenging allows cancer cells to remain in the tumorigenic range of ROS levels. Activation of mitochondrial ROS generation by oncogenes, mitochondrial mutations, hypoxia, or tumor suppressor loss increases ROS signaling to increase tumorigenicity. Tumor cells also express enhanced levels of antioxidant proteins that prevent increased ROS from reaching cytotoxic levels incompatible with growth (24).

cells. On the other hand, there are some other pathways within the tumor cell to scavenge the extra

ROS. Balanced between the generation and scavenge effect, the ROS is at the level higher than that in cytostatic, but lower than cytotoxic, that is at the tumorigenic level (24). This is illustrated as Figure. 5.

With new ROS and other chemical radicals generated by the irradiation, the overall toxic chemical species can be out of the tolerance of the tumor cells. One direct effect is irreparable cell damage, and a consequence of apoptosis. It is then quite important to quantify different chemical species within the cellular nucleus after irradiation.

Table 1. The summary of the state-of-the-art experimental measurements for IR induced DNA damage. σ and $d\sigma$ represent the total and the differential cross sections, respectively.

Stages	Main findings		
Overall[5]	The cell survival curve is found physical dose, dose rate, LET, particle trajectory and oxygen concentration dependent. Low energy electron is found DNA damage significant.		
Physics[25-33]	**IR type (energy range)**	**σ in gaseous water**	**$d\sigma$ in water vapor**
	Electron (10 eV-keV)	Elastic; ionization	Elastic; ionization
	Proton (keV-MeV)	Electron capture/loss; ionization	Ionization
	Helium (keV-MeV)	Excitation + ionization;	
Physicochemical	No measurement		
Chemical	Rich data in water solvent, while rare data in cellular surroundings.		
DNA damage[34, 35]	Lethal DNA damage related: SSBs, DSBs, DNA-DNA and DNA-protein cross-links, base release and other chemical modifications; Quantitative measurement: SSBs and DSBs at the kilobase precision level*.		
Note: SSBs: single strand breaks; DSBs: double strand breaks;			

1.4 Challenges to quantify the oxygen effect in the chemical stage

In the past several decades, there have been great efforts to measure the total and differential cross sections between IR and water molecules and the chemical reactions and diffusions of the relevant radicals. The so-far progress has been summarized in Table 1. It is clear that, there have accumulated rich experimental data in both fundamental process measurement and DNA damage quantification.

More specific to the chemical reaction and diffusion, multiple parameters were derived from the raw measurement to quantify the process. As shown in Table 2, the diffusion coefficient (D) and radii (R) for common chemical species, including the initial generation from the physicochemical process, those dissolved in the water solvent, and the induced species from mutual interactions have been derived from previous work (36). The full mutual interaction among these radicals are then listed in Table 3. In this Table, α is defined as

Table 2. Diffusion coefficients and radii of radiolytic species (36).

Species	D (10^9 nm^{2}s^{-1})	R (nm)	Species	D (10^9 nm^{2}s^{-1})	R (nm)
$H^{\cdot}$	7.0	0.19	$O_2^{\cdot-}$	1.75	0.22
$^{\cdot}OH$	2.2	0.22	$HO_2^{\cdot}$	2.3	0.21
H_2O_2	2.3	0.21	HO_2^-	1.4	0.25
H_2	4.8	0.14	$O(^3P)$	2.0	0.20
e_{aq}^-	4.9	0.50	$O^{\cdot-}$	2.0	0.25
H^+	9.46	0.25	$O_3^{\cdot-}$	2.0	0.20
OH^-	5.3	0.33	O_3	2.0	0.20
O_2	2.4	0.17			

$$\alpha = \frac{k_{act} + 4\pi RD}{4\pi R^2 D}.$$

With it and other parameters listed in Table 3, the probability of reaction is determined as

Table 3. Mutual reactions in terms of reaction rate constants ($k_{obs}, k_{dif}, k_{act}$), reaction radii (R), probability of geminate recombination and alpha (definition given in text) (36).

Reaction	k_{obs} (M^{-1} s^{-1})	R (nm)	k_{dif} (M^{-1} s^{-1})	k_{act} (M^{-1} s^{-1})	P_{React}	α (nm^{-1})
$H^{\cdot} + {}^{\cdot}OH \rightarrow H_2O$	1.55×10^{10}	0.41	2.86×10^{10}	3.40×10^{10}	0.33	5.34
$H^{\cdot} + H_2O_2 \rightarrow H_2O + {}^{\cdot}OH$	3.50×10^{7}	0.40	2.82×10^{10}	3.50×10^{7}	0.00	2.50
$H^{\cdot} + OH^- \rightarrow H_2O + e_{aq}^-$	2.51×10^{7}	0.52	4.84×10^{10}	2.51×10^{10}	0.00	1.92
$H^{\cdot} + O_2 \rightarrow HO_2^{\cdot}$	2.10×10^{10}	0.36	2.56×10^{10}	1.17×10^{11}	0.67	15.4
$H^{\cdot} + HO_2^{\cdot} \rightarrow H_2O_2$	1.00×10^{10}	0.40	2.82×10^{10}	1.55×10^{10}	0.19	3.88
$H^{\cdot} + O_2^{\cdot-} \rightarrow HO_2^-$	1.00×10^{10}	0.41	2.72×10^{10}	1.58×10^{10}	0.20	3.86
${}^{\cdot}OH + {}^{\cdot}OH \rightarrow H_2O_2$	5.50×10^{9}	0.44	7.32×10^{9}	2.21×10^{10}	0.55	9.14
${}^{\cdot}OH + H_2O_2 \rightarrow HO_2^{\cdot} + H_2O$	2.88×10^{7}	0.43	1.46×10^{10}	2.88×10^{7}	0.00	2.33
${}^{\cdot}OH + H_2 \rightarrow H^{\cdot} + H_2O$	3.28×10^{7}	0.36	1.91×10^{10}	3.29×10^{7}	0.00	2.78
${}^{\cdot}OH + e_{aq}^- \rightarrow OH^-$	2.95×10^{10}	0.72	3.87×10^{10}	1.25×10^{11}	0.49	5.87
${}^{\cdot}OH + OH^- \rightarrow O^{\cdot-} + H_2O$	6.30×10^{9}	0.55	3.12×10^{10}	7.90×10^{9}	0.08	2.28
${}^{\cdot}OH + HO_2^{\cdot} \rightarrow O_2 + H_2O$	7.90×10^{9}	0.43	1.46×10^{10}	1.72×10^{10}	0.33	5.05
${}^{\cdot}OH + O_2^{\cdot-} \rightarrow O_2 + OH^-$	1.07×10^{10}	0.44	1.32×10^{10}	5.76×10^{10}	0.64	12.2
${}^{\cdot}OH + HO_2^- \rightarrow HO_2^{\cdot} + OH^-$	8.32×10^{9}	0.47	1.28×10^{10}	2.38×10^{10}	0.42	6.08
${}^{\cdot}OH + O^{\cdot-} \rightarrow HO_2^-$	1.00×10^{9}	0.47	1.49×10^{10}	1.07×10^{9}	0.03	2.28
${}^{\cdot}OH + O_3^{\cdot-} \rightarrow O_2^{\cdot-} + HO_2^{\cdot}$	8.50×10^{9}	0.42	1.34×10^{10}	2.34×10^{10}	0.42	6.55
$H_2O_2 + e_{aq}^- \rightarrow OH^- + {}^{\cdot}OH$	1.10×10^{10}	0.71	3.87×10^{10}	1.54×10^{10}	0.11	1.97
$H_2O_2 + OH^- \rightarrow HO_2^- + H_2O$	4.71×10^{8}	0.54	3.11×10^{10}	4.78×10^{8}	0.01	1.88
$H_2O_2 + O(^3P) \rightarrow HO_2^{\cdot} + {}^{\cdot}OH$	1.60×10^{9}	0.41	1.33×10^{10}	1.82×10^{9}	0.05	2.77
$H_2O_2 + O^{\cdot-} \rightarrow HO_2^{\cdot} + OH^-$	5.55×10^{8}	0.46	1.50×10^{10}	5.76×10^{8}	0.01	2.26
$H_2 + O(^3P) \rightarrow H^{\cdot} + {}^{\cdot}OH$	4.77×10^{3}	0.34	1.75×10^{10}	4.77×10^{3}	0.00	2.94
$H_2 + O^{\cdot-} \rightarrow H^{\cdot} + OH^-$	1.21×10^{8}	0.39	2.01×10^{10}	1.22×10^{8}	0.00	2.58
$e_{aq}^- + O_2 \rightarrow O_2^{\cdot-}$	1.74×10^{10}	0.67	3.70×10^{10}	3.23×10^{10}	0.22	2.79
$e_{aq}^- + HO_2^{\cdot} \rightarrow HO_2^-$	1.29×10^{10}	0.71	3.87×10^{10}	1.92×10^{10}	0.13	2.11
$OH^- + HO_2^{\cdot} \rightarrow O_2^{\cdot-} + H_2O$	6.30×10^{9}	0.54	3.11×10^{10}	7.91×10^{9}	0.08	2.32
$OH^- + O(^3P) \rightarrow HO_2^-$	4.20×10^{8}	0.53	2.93×10^{10}	4.26×10^{8}	0.01	1.91
$O_2 + O(^3P) \rightarrow O_3$	4.00×10^{9}	0.37	1.23×10^{10}	5.92×10^{9}	0.18	4.00
$O_2 + O^{\cdot-} \rightarrow O_3^-$	3.70×10^{9}	0.42	1.40×10^{10}	5.03×10^{9}	0.13	3.24
$HO_2^{\cdot} + HO_2^{\cdot} \rightarrow H_2O_2 + O_2$	9.80×10^{5}	0.42	7.31×10^{9}	9.80×10^{5}	0.00	2.38
$HO_2^{\cdot} + O_2^{\cdot-} \rightarrow HO_2^- + O_2$	9.70×10^{7}	0.43	1.32×10^{10}	9.77×10^{7}	0.00	2.34
$HO_2^- + O(^3P) \rightarrow O_2^{\cdot-} + {}^{\cdot}OH$	5.30×10^{9}	0.45	1.16×10^{10}	9.77×10^{9}	0.25	4.10

$$P_{\mathrm{II}}(t|r_0) = \frac{k_{\mathrm{act}}}{4\pi R D r_0 \alpha}\left[\mathrm{Erfc}\left(\frac{r_0 - R}{\sqrt{4Dt}}\right) - W\left(\frac{r_0 - R}{\sqrt{4Dt}}, \alpha\sqrt{Dt}\right)\right]$$

With the information formed in Tables 2 and 3, in principle, we could tackle the hypothesis of oxygen reaction effect for the OER phenomena via a step-by-step simulation. Microscopic Monte Carlo (MC) simulation, a numerical computer simulation technique, using statistical resampling method to solve complex systems that have no easy analytical solutions, has been a useful toolkit to perform relevant computations in a multi-spatiotemporal scale fashion (37). Over the past two

decades, there have been multiple microscopic MC simulation packages developed for this purpose (5, 25, 38-45), such as TRAX, PARTRAC, Geant4-DNA, RITRACKS, etc.

Despite the success, it is quite challenging to simulate the oxygen effect in a step-by-step fashion. The rationale is as follows. The chemical stage spans from pico- to micro- seconds. The radicals then need be diffused for tremendous time steps before the stage ends. They will also react with each other, as well as with surrounding background water molecules. This leads to a many-body simulation problem, for which the computational complexity scales with N^2, where N is the number of radicals. It is found that the radical generated from the physicochemical stage can be a huge amount. It can produce 10^5 radicals per 1 MeV energy deposition (22). These two terms then make it computationally super-expensive to transport and simulate the chemical reactions among radicals. Once the dissolved oxygen was considered into the chemical stage in a step-by-step manner, the computational costs would be increased by several orders (22). This heavy computational burden makes it almost impossible for the state-of-the-art MC tools to fully examine this process.

To reduce the computational burden, the oxygen is sometimes ignored (46, 47) or treated as a temporally constant and spatially uniform background (48, 49) that serves as a scavenger for the radiolytic radicals. The method assuming a constant uniform background ignores the spatial and temporal variations of chemical reactions, an important factor in certain scenarios. For instance, when rapid consumptions of oxygen due to reactions with radicals occur, temporal variation of oxygen concentration may not be omitted. Meanwhile, as the oxygen distribution is sparse compared to the very short reaction radii, reactions with oxygen happens non-uniformly, making spatial variation a factor to consider.

Recent, in our group, an open-source (https://github.com/utaresearch/gMicroMC) GPU-based MC simulation package, gMicroMC, for the simulations of water radiolysis and computations of DNA damages has been developed (50). In which, the GPU acceleration technology can improve computational efficiency by hundreds of times compared to conventional CPU-based computations in the context of microscopic MC simulation. Upon it, quite recently, our group enabled the step-by-step simulation of the oxygen effect.

Since the oxygen simulation module is newly developed, the purpose of this thesis is of two aspects. First, through performing multiple simulations using gMicroMC, we will try to test of the robustness of the code under various oxygen levels and test the user-friendly property via recording those "easy-to-misunderstand" points. Second, we will examine the chemical radical evolution under various oxygen levels for proton therapy with various energies. Through which, we could quantify the oxygen depletion effect contributing to the OER effect.

CHAPTER 2: METHODS AND MATERIALS

We used GPU based inhouse developed gMicroMC package to study the yield of ROS at different concentration of oxygen.

2.1 Introduction of gMicroMC

Microscopic Monte Carlo (MC) simulation of the water radiolysis, as well as the computation of biologically relevant quantities such as DNA damages, is of critical importance for the understanding of microscopic basis of radiation effects. It is usually divided into four steps: physical stage for transportation of source particles and production of ionized and excited water molecules, physicochemical stage for generation of initial radicals from the ionized and excited water molecules, chemical stage for diffusion and reaction between radicals and finally analysis of DNA damage from the position of energy deposition events and radicals. gMicroMC (50), a novel GPU-based microscopic MC simulation package, has made these four steps capable of being simulated by GPU (**Error! Reference source not found.**), making it computationally efficient. Therefore, it enables the systematic study on many different conditions and the variation of their results, giving comprehensive analysis. Here, we will briefly introduce the models used by gMicroMC and the GPU implementation in different stages. Interested readers should refer to the reference (50, 51) for more information.

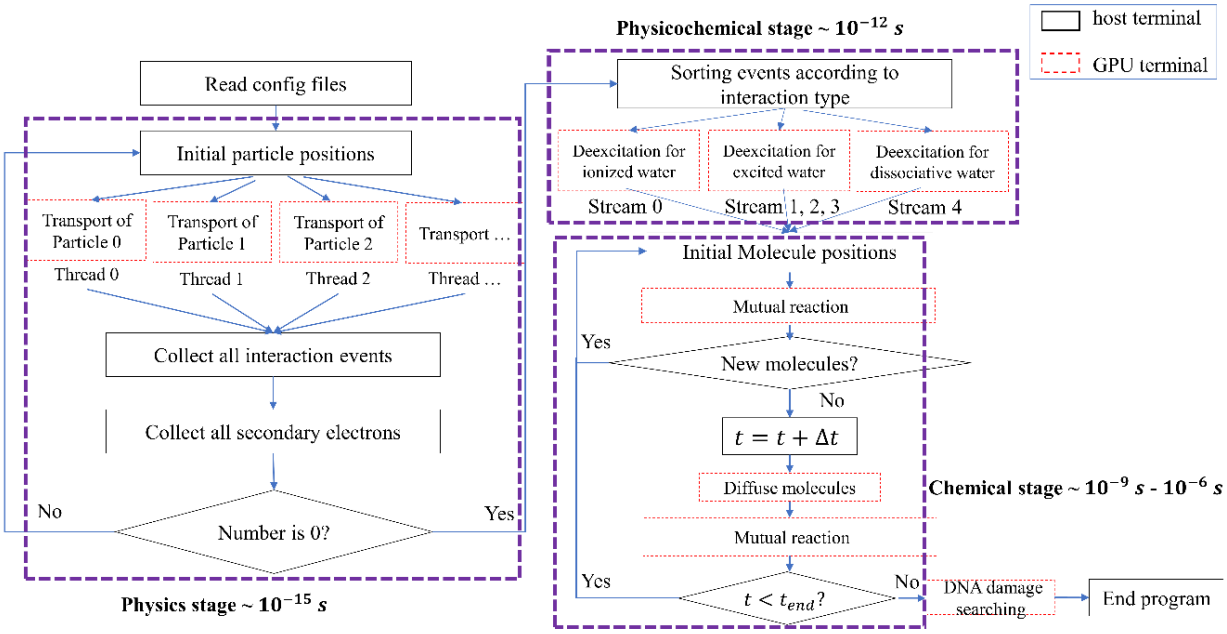

Figure 2.1 Workflow of gMicroMC

2.1.1 Physical stage

gMicroMC initially only support electrons as source particles. In this stage, an electron will undergo different types of physical interaction with water molecules, until its energy falls below the predefined cutoff energy, where the energy will be regarded as being deposited locally and entirely at one time. Four types of interaction are considered: ionization, excitation, elastic collision, and dissociative electron attachment, i.e., electrons can lose energy or change the direction through these four interactions. Five different shells of water molecules (molecular orbitals) were considered for ionization interaction and the relativistic extension of the binary-encounter-Bethe (rBEB) model (52, 53) was used to compute ionization cross sections for electrons with energy ranging from 10 eV to 100 MeV. The electron binding energies came from

the work of Dingfelder *et al* (54). As for excitation, the semi-analytic model introduced by Olivero et al (55) was employed. Five types of excitation levels of A^1B^1, B^1A^1, Rydberg A+B, Rydberg C+D and diffusion were considered and the excitation energy for different levels came from the work of Dingfelder *et al* (54). The cross section of elastic interaction was divided into two part according to the energy of incident electrons. The semi-empirical differential cross sections of Brenner and Zaider (56) and Rutherford formula (57) were applied for energy below 200 eV and above 200 eV, respectively. The former one is actually a parameterized expression with adjustable parameters determined by fitting to experimental data, because Rutherford formula deviates from the experiment data for low energy electrons. Finally, study (58) showed that radicals can still be generated even if the energy of incident electrons is lower that the lowest energy of ionization and excitation through dissociative attachment. The cross-section data of dissociative attachment were extracted from this work.

After having the cross-section data for all channels, the sampling of physics track of electrons was done accordingly. The distance s to the next interaction is sampled by $s = -\frac{1}{\rho \sum_i \sigma_i} \ln \zeta$, where ρ is the density of water, σ_i the cross section data for a specific interactions and subtypes indexed by i and ζ a random number uniformly distributed in $[0,1]$. After advancing the electron by s, we sampled the interaction type and subtype based on the relative weight of $\sigma_i / \sum_i \sigma_i$. For an ionization event, the energy of the secondary electron was determined by means of the composition sampling method, which was developed originally in CPA100 code (59, 60). The scattering angle θ_p of primary electron for both an ionization and an excitation event was computed as $\sin^2 \theta_p = \frac{(W/T)}{(1-W/T)T/(2m_0c^2)+1}$, where W and T are energy loss of the primary electron and its energy before the event, respectively. m_0 and c are the rest mass of an electron and the speed of light. As for the

secondary electron generated from the ionization process, the ejection angle θ_s followed $\sin^2\theta_s = \frac{1-W/T}{1+W/(2m_0c^2)}$ for $W > 200\ eV$. θ_s uniformly distributed in $[\pi/4, \pi/2]$ with a 90% probability and in $[0, \pi]$ for the rest 10% probability, when $50eV < W < 200\ eV$. For $W < 50\ eV$, θ_s uniformly distributed in $[0, \pi]$. For an elastic collision event, the primary electron did not have energy loss and the scattering angle was sampled using the inverse transform method (61). As for the dissociative attachment reactions, the primary electron disappeared, and dissociative water molecules were produced.

The above cross section data is tabulated into lookup tables that can be read into GPU memory, rather than being calculated on the fly, for efficiency improvement. Linear interpolation was used for energy between the tabulated energy values. In this stage, each GPU thread was responsible for simulating the transport of one incident electron and recording its secondary electrons. In next run, the secondary electrons will be simulated by the kernel until no secondary electrons are produced.

In this work, we simulated proton instead. To achieve this goal, a module that deal with proton was developed and integrated with the one dealing with electrons. The proton module only considered ionization and excitation interactions between protons and water molecules. The model was adopted from Ianik's work (62). The yields of radicals were compared to other publications and it agreed well within 10% difference. But the data were not published and peer-reviewed. This work will do the comparison too and hence is a validation of the module as well. The implementation of GPU was changed as well. The kernel will now run simulation for proton first to avoid thread divergence and then followed by the kernel deal with electrons.

2.1.2 Physicochemical stage

Table 4. Branching ratios for ionized and excited water molecules used in gMicroMC

		Pathway	Decay channel	Branching ratios (%)
Ionized water molecules	$1b_1$, $3a_1$, $1b_2$, $2a_1$, K	Dissociation	$H_3O^+ + \cdot OH$	100
Excited water molecules	A^1B^1	Dissociation	$\cdot OH + H \cdot$	65
		Relaxation	$H_2O + \Delta E$	35
	B^1A^1	Auto-ionization	$H_3O^+ + \cdot OH + e_{aq}^-$	55
		Dissociation	$H_2 + \cdot O \cdot$	15
		Relaxation	$H_2O + \Delta E$	30
	Rydberg A+B, Rydberg C+D and diffusion	Auto-ionization	$H_3O^+ + \cdot OH + e_{aq}^-$	50
		Relaxation	$H_2O + \Delta E$	50

The physical stage determines the initial types and positions of ionized or excited water molecules. These water molecules should de-excite through some channels, which in gMicrMC is the same model as PARTRAC (63). Depending on different types, the pathways and their probabilities changed as well. The pathways are summarized in Table 4. Sub-excitation electrons transferred their excess energy to the surrounding medium until thermal energies through a number of inelastic processes. The thermalization displacement r was sampled according to a distribution $f(r) = 4r \exp(-2r)$, where the unit of r is nm. At the end of the thermalization process, a low energy sub-excitation electron formed a cluster in aqueous solution by attaching surrounding water molecules. Since the pathway of ionized and excited water molecules and the thermalization of

Table 5. Radical species and diffusion coefficients D. The root-mean-square distance λ traveled for $t = 1\ \mu s$ was calculated as $\lambda = \sqrt{6Dt}$.

	Species	D (x$10^9\ nm^2 s^{-1}$)	λ (nm)	Reference
Existing in original gMicroMC	e_h	4.9	171.5	(63)
	$OH\cdot$	2.8	129.6	(63)
	$H\cdot$	7.0	204.9	(63)
	H^+	9.0	232.4	(63)
	H_2	4.8	169.7	(63)
	OH^-	5.0	173.2	(63)
	H_2O_2	2.3	117.5	(63)
Added in this work	O_2	2.4	120.0	(64)
	$HO_2^{\cdot}$	2.3	117.5	(64)
	$O_2^{\cdot -}$	1.75	102.5	(64)
	HO_2^-	1.4	91.7	(64)

sub-excitation electrons are independent, the water molecules are first sorted by their types and grouped by the decay pathway. Then, CUDA streams are created to deal with different decay pathway asynchronously. For each stream, multi GPU thread is used to deal with specific water molecules.

2.1.3 Chemical stage

The chemical stage of water radiolysis is modelled in a step-by-step fashion. It consists of two types of chemical kinetics: diffusion of the radiolytic molecules during the time step and the check of their mutual chemical reactions after one-time step. The diffusion is a simple three-dimensional Gaussian sampling with standard deviation related to diffusion constant and time step. The check for mutual reaction is a little bit more complicated due to mutual competitive chemical reactions between radiolytic molecules. The grid data approach was employed, where the entire space was

divided into small grids with the grid size being twice of the largest reaction distance. In this way, each radical in a grid can only react with other radicals in the same grid or those around it. This strategy substantially reduced the computation complexity because of much fewer reactions to consider. Implementation details can be found in our previous publication (65).

The initial development of gMicroMC did not include oxygen in the simulation process. To enable this feature, oxygen-related reactions with parameters listed in previously published studies (64) were added. Because of the absence of $O^{\cdot -}$, O_3, $O_3^{\cdot -}$, $O(3P)$ in the physicochemical stage, only three radicals in addition to those already included in the original gMicroMC, namely hydroperoxyl radical $HO_2^{\cdot}$, superoxide radical $O_2^{\cdot -}$ and hydroperoxide anion HO_2^-, were considered additionally. All the chemical species in this study are listed in Table 5. The existence of oxygen was assumed to not affect the physical stage and the physicochemical stage. In fact, the concentration of water molecule is ~55.6 MM but the concentration of dissolved oxygen is ~0.2 mM for $P_{o_2} = 21\%$. Hence, the probability for the incident initial particles to collide with dissolved oxygen in the physical stage is low and can be safely ignored. Hence, the inclusion of oxygen into gMicroMC is very straightforward and will not cause problems as long as the extra reactions for oxygen and radicals in chemical stage follow the same rules. The updated reaction lists are shown in Table **6**.

Table 6. Chemical reactions and reaction rate constants k_{obs}. H_2O molecules were ignored in the chemical equations assuming they were everywhere.

	Index	Reaction channels	k_{obs} ($10^{10}\ L \cdot mol^{-1} \cdot s^{-1}$)
Existing in original gMicroMC	1	$e_h + e_h \rightarrow 2OH^- + H_2$	0.5
	2	$e_h + OH\cdot \rightarrow OH^-$	2.95
	3	$e_h + H\cdot \rightarrow OH^- + H_2$	2.65
	4	$e_h + H^+ \rightarrow H\cdot$	2.11
	5	$e_h + H_2O_2 \rightarrow OH\cdot + OH^-$	1.41
	6	$OH\cdot + OH\cdot \rightarrow H_2O_2$	0.44
	7	$OH\cdot + H\cdot \rightarrow H_2O$	1.44
	8	$H\cdot + H\cdot \rightarrow H_2$	1.20
	9	$H^+ + OH^- \rightarrow H_2O$	14.3
	10	$H_2 + OH\cdot \rightarrow H\cdot$	0.00417
Added in this work	11	$e_h + O_2 \rightarrow O_2^-$	1.74
	12	$e_h + HO_2 \rightarrow HO_2^-$	1.29
	13	$e_h + O_2^- \rightarrow 2OH^- + H_2O_2$	1.29
	14	$OH\cdot + HO_2 \rightarrow O_2$	0.79
	15	$OH\cdot + O_2^- \rightarrow O_2 + OH^-$	1.07
	16	$OH\cdot + HO_2^- \rightarrow HO_2 + OH^-$	0.832
	17	$H\cdot + O_2 \rightarrow HO_2$	2.1
	18	$H\cdot + HO_2 \rightarrow H_2O_2$	1.0
	19	$H\cdot + O_2^- \rightarrow HO_2^-$	1.0
	20	$H^+ + O_2^- \rightarrow HO_2$	4.78
	21	$H^+ + HO_2^- \rightarrow H_2O_2$	5.0

2.1.4 DNA damage searching

To determine whether a DNA damage occurs, we need to build a DNA model for checking the damage sites. The DNA model is shown in Figure , which is extracted from reference (50). The

chromatin fiber unit (Figure (d1) and (d2)) is used to fill the cell nucleus randomly and smoothly (50, 66). The DNA model contained ~6.2 Gbp nucleotides.

The first step of DNA damage calculation was to calculate strand breaks (SBs) caused by physical events (direct damages) or radicals (indirect damages). This was a highly parallelizable job favored by GPU. As such, each GPU thread was responsible for one physical event or one radical to determine whether it induced a damage. This was achieved by searching through the DNA model and checking whether the point coordinate fell inside a sugar-phosphate group. Due to the multi-scale structure of the DNA model, the search was performed from the coarsest to the finest scale. The criteria for judging that one events fall inside the DNA model depends on many parameters and readers should find corresponding value in reference (50). The second step of DNA damage calculation was to compute damages of different levels of complexities. This step is actually done in CPU since it cost little time even grouping them in order.

2.2 Simulation setup

The general idea of simulation is to compare the oxygen effect from gMicroMC to that obtained from the continuous background method (48).

In Boscolo *et al* (48)'s work, oxygen effect was studied for proton beams with multiple incident energies and positions with different linear energy transfers (LETs). In dosimetry, LET is the amount of energy that an ionizing particle transfers to the material traversed per unit distance. It describes the action of radiation into matter. Since in gMicroMC, the input parameters are not

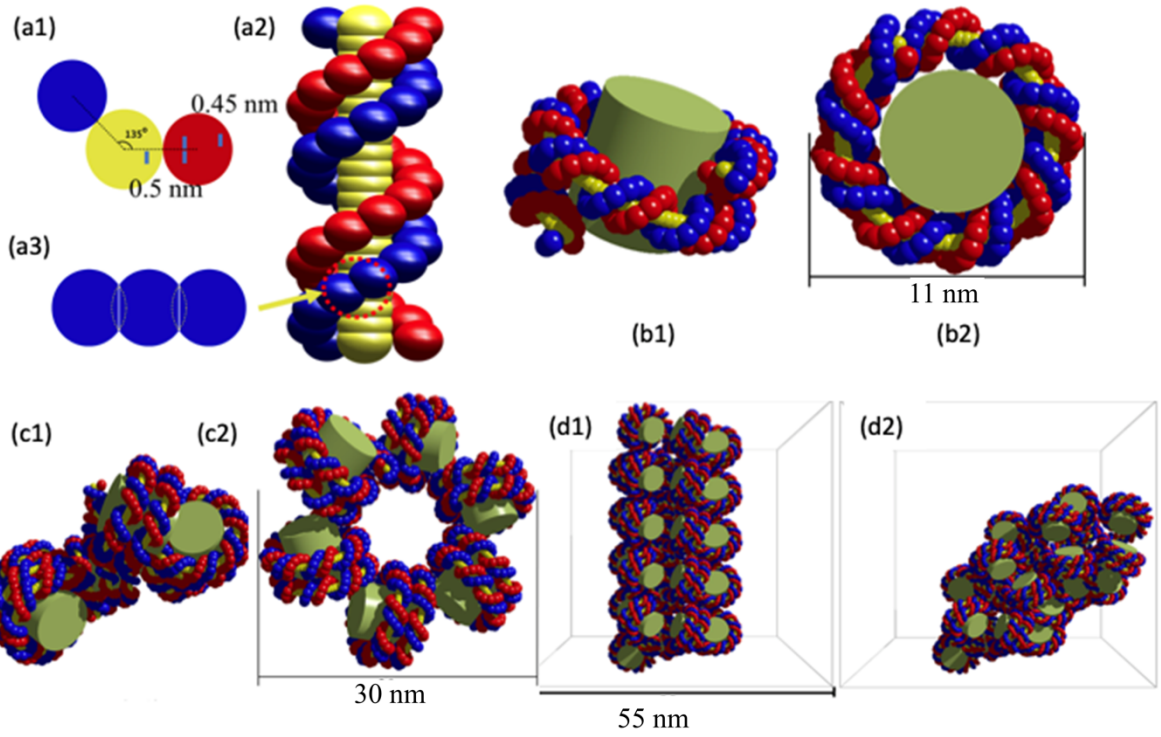

Figure 2.2 (a1) The nucleotide pair including a base pair (yellow) and two sugar-phosphate groups (blue and red), (a2) a B-DNA segment, and (a3) the overlap between two neighboring groups. (b1) (b2) Nucleosome structure. (c1) (c2) Chromatin fiber loop. (d1) A straight chromatin fiber unit and (d2) a bent chromatin fiber unit. (wileyonlinelibrary)

directly LET dependent, we then first simulate the LET distribution of proton beams entering into a water phantom. After that, we obtain the corresponding depth positions for the interested LET

values and set up the region of interest (ROI) based on it. The LET simulation was performed with Geatn4 MC simulation tool.

The ROI is a $5 \times 5 \times 5\ \mu m^3$ cube centered at the origin. Based on the depth position d obtained from the Geant4 simulation, the proton starting plane in the gMicroMC was then set d away from one side of the ROI, and then travels towards the ROI with the corresponding initial kinetic energy. The starting position of proton uniformly locates on a $5 \times 5\ \mu m^2$ plane (Figure). Physical stage was then simulated for the whole track, but subsequent physicochemical would be restricted in ROI. The following chemical stage was done at oxygen levels P_{O_2} of 0, 3%, 7% and 21%. The oxygen was uniformly sampled inside ROI, with its number being calculated by $N_{O_2} = P_{O_2} * P_{atm} * H_c * N_A * V$. $P_{atm} = 760\ mmHg$ represents the atmosphere pressure. $H_c = 1.26\ \mu mol * L^{-1} * mmHg^{-1}$ is the coefficient of Henry's Law for oxygen dissolving in water (67). $N_A = 6.023 \times 10^{23}/mol$ is the Avogadro constant. $V = 5 \times 5 \times 5\ \mu m^3$ represents the volume of ROI. During the simulation, we recorded the yield, or G value, of different radicals. The G value calculates the ratio between the number of molecules of the chemical species and the deposited energy to generate such a number of molecules in the unit of $\#\ of\ molecules/100\ eV$. Due to the stochastic feature of MC simulation, the sampling and simulation was continued until the energy in ROI reaches 2.5 *MeV* (to be consistent with Boscolo *et al* (48)). Hence, an average was done on G values over multiple primary protons. The temporal length of chemical stage is 1 μs. The averaged G values were then compared to the data gathered by Boscolo *et al* (48). Two energies of proton beam were chosen, namely 10 *MeV* and 90 *MeV*.

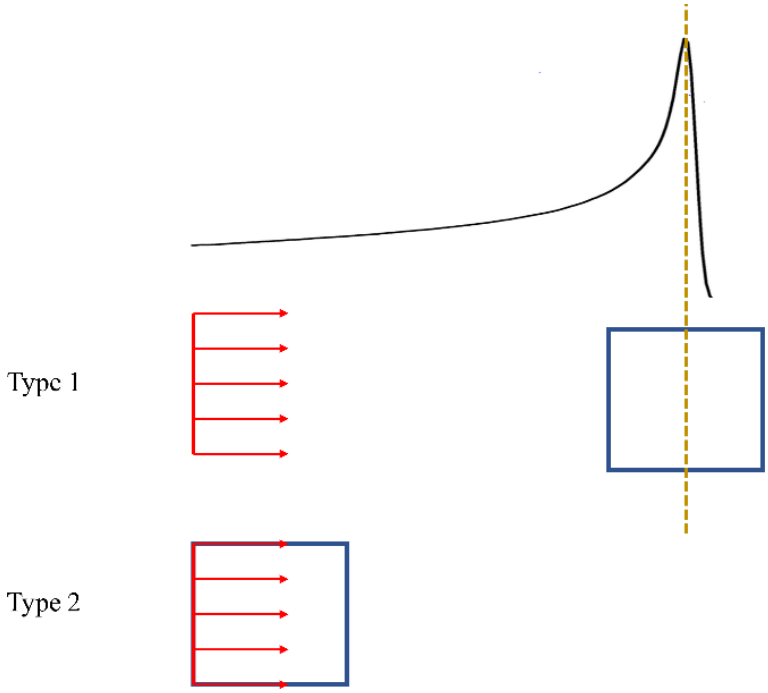

Figure 2.3 illustration of the cross section of the two simulation setups. The top curve represents dose-depth behavior of proton (Bragg peak). The box means ROI and the arrows represent the staring positions and directions of protons.

2.3 Error documenting as a fresh user of gMicroMC

Since gMicroMC is an in-house developed simulation software by our research group and collaborators in University of Texas Southwestern Medical Center (UTSW), a thorough evaluation of its performance and user-experience would be valuable before it was released to a broad research community for a broader impact. Hence, in this thesis, we also documented the errors and easy-to-make-mistakes during the application of gMicroMC on studying on the oxygen effect for proton therapy. We will then also provide our solutions in solving these problems

CHAPTER 3: RESULTS AND DISCUSSION

3.1 Simulation results

3.1.1 LET and depth position of the proton beam

In Boscolo et al's work, radiolytic yields of different chemical species at different oxygenation condition by 10 MeV proton beam with LET=3.9 keV/μm, and by 90 MeV proton beam with LET = 0.56 keV/ μm were studied. Using Geant4 simulation, we found these LET values corresponds to the entrance part of the corresponding proton beams (the 10 MeV one was shown in Figure 9). Hence, in gMicroMC, one side of ROI box was then placed coincident with that of the proton initialization plane.

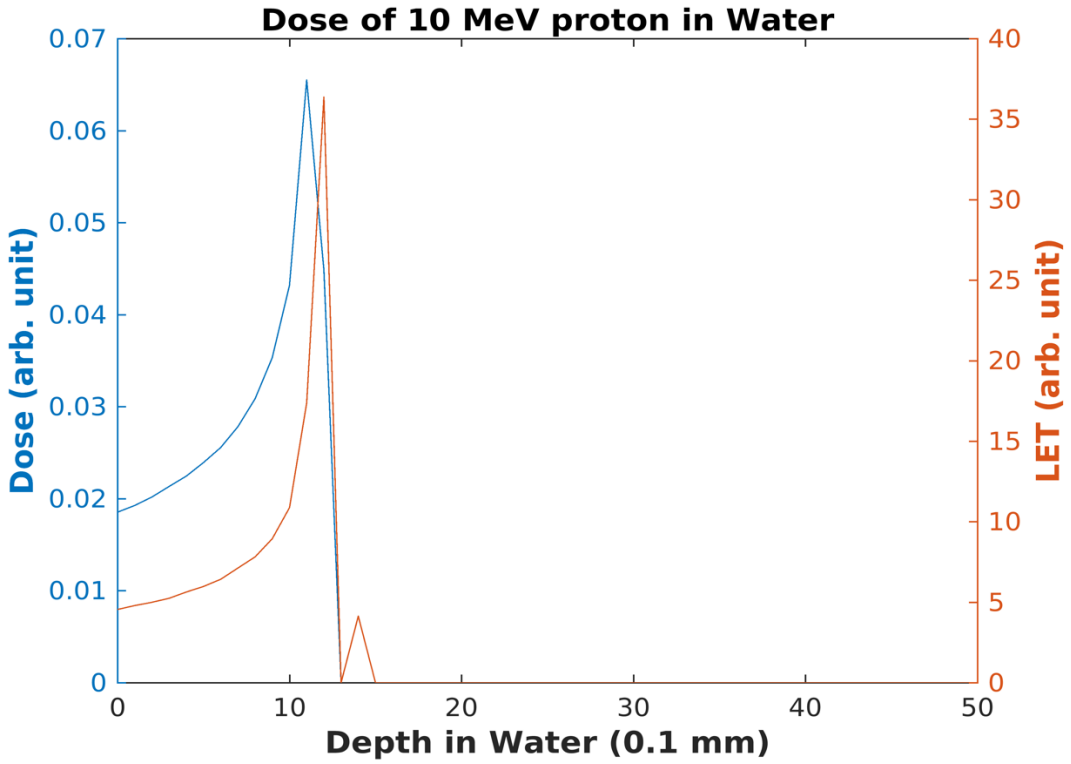

Figure 3.1 The dose profile and LET of the 10 MeV proton beam penetrating a water phantom.

3.1.2 Radiolysis of Oxygenated Water under 90 MeV proton irradiation

This first set of results shows the time-dependent yield of different chemical species for targets with different oxygen levels in the time interval of 10^{-12} to10^{-6} s. These results show the chemical evolution of 90 MeV proton radiation.

3.1.2.1 Results at oxygen concentration level at 0%

This first figure (Figure 10) is done at an oxygen concertation level of 0%. In the early stages electrons and OH are the most abundant chemical species. As time progresses, the number of electrons and OH radicals decrease. Since there is no oxygen present in the target, the surrounding electrons cannot create O_2^- or HO_2 when it ionizes the water. This does not mean that we have no ROS production at this stage. H_2O_2 is produced due to mutual interactions among radicals. Also, OH is produced and is the most abundant by product at this stage. The amount of hydrogen atom present at all time intervals seems to be relatively constant.

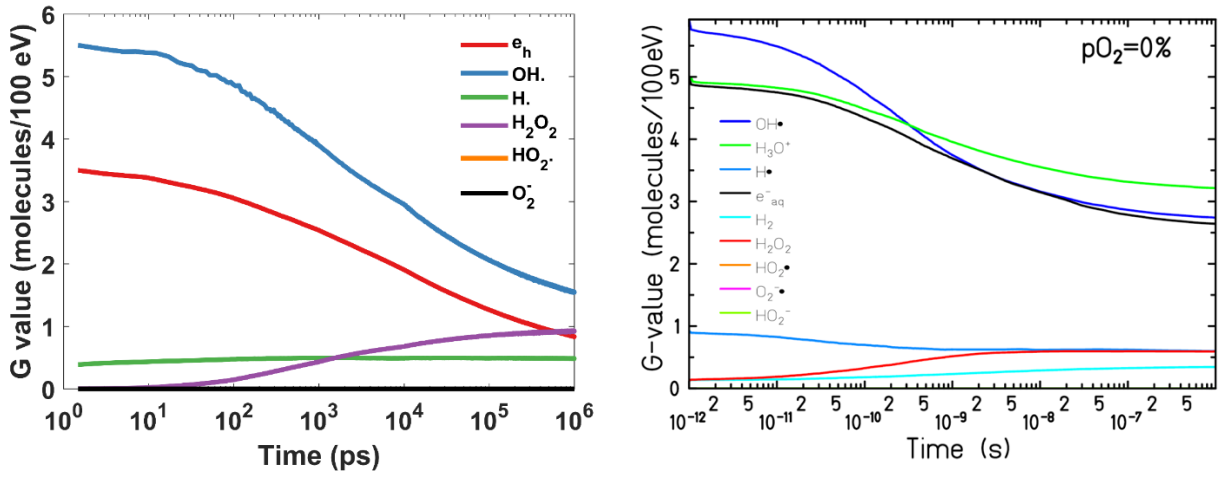

Figure 3.2 Time dependent yield of the chemical species generated by a 90 MeV proton track in an oxygenated target in equilibrium with an atmospheric partial oxygen pressure at the water surface of 0%. Left: from gMicroMC; Right: from work of Boscolo *et. al.* (48).

Compared to that from the work of Boscolo et. al. (48), the overall time evolution of the yielding of the simulated chemical species is similar. Yet, there are also some differences. One

noticeable difference is with the free electron radicals. The G-value of electrons at the beginning of the chemical stage is around 3.5 from gMicroMC, while it is around 4.8 reported by Boscolo *et al.* At the end of the chemical stage simulation, the G-value of the electrons dropped to around 1 while that from Boscolo *et al.* was around 2.6. Another noticeable difference is the slope for the time evolution curve for each species. After ~ 100 ps, the G values for electron radical, OH radical and H_2O_2 changed much faster in gMicroMC than that from the work of Boscolo *et al*. This can be caused by different reaction rates applied in the two simulation packages.

3.1.2.2 Results at oxygen concentration level at 3%

In Figure 11, the oxygen concentration level of the target is at 3% is presented. Just as before, the most abundant by products at this time are electron radical and $OH^{\cdot}$ At this stage much more drastic consumption of electron radical is noticeable. Hydrogen atom also starts to be consumed at this oxygen concentration level. At the end of the chemical stage, the production of O_2^{-} and $HO_2^{\cdot}$ can also been seen. This is due to the electrons having more oxygen to interact with. So, when the water is now ionized, the oxygen can now bond with the free electron or the hydrogen atom creating O_2^{-} and $HO_2^{\cdot}$. However, at this level of oxygen concentration, the amount of both of these products is still relatively small. The amount of H_2O_2 remains relatively the same when compared to the previous oxygen concentration level of 0%.

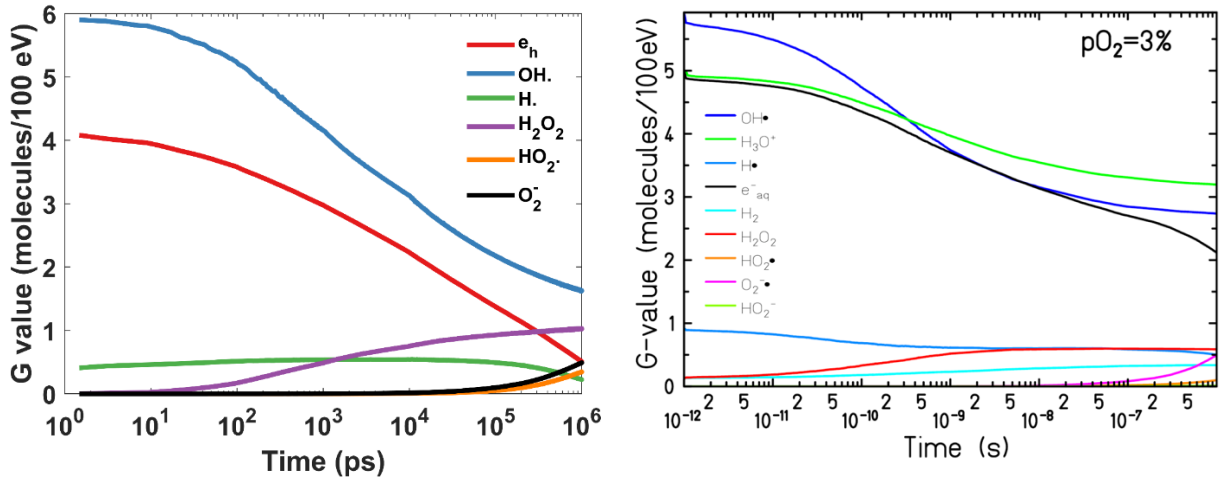

Figure 3.3 Time dependent yield of the chemical species generated by a 90 MeV proton track in an oxygenated target in equilibrium with an atmospheric partial oxygen pressure at the water surface of 3%. Left: from gMicroMC; Right: from work of Boscolo *et. al.* (48).

3.1.2.3 Results at oxygen concentration level at 7%

In this setup the oxygen concentration level is now at 7%. The results are as shown in Figure 12. As like the previous concentration level, at the beginning of the chemical stage, electrons and OH are the most produced chemical species at this point. At the beginning of the chemical stage, little to no O_2^-, $HO_2\cdot$ and H_2O_2 are produced. Also, hardly any hydrogen atom is produced as well. The consumption rate for the electrons and hydrogen atom at 1 ns also seem to be the same as the other lower oxygen concentration levels. The total number of electrons consumed at the final chemical stage is much smaller than the other lower concentration levels. This is due to having more oxygen particles to interact with. In theory with enough oxygen around, all of the electrons would be consumed in order to create ROS. The amount of H_2O_2 produced is unaffected by the change in oxygen concentration. At the end of the chemical stage, almost all of the hydrogen atom is consumed. Since more electrons and hydrogen radicals are consumed, there

is an increase of the amount of O_2^- and $HO_2^\cdot$ created. However, the amount of OH radical produced seems to be the same as the previous results.

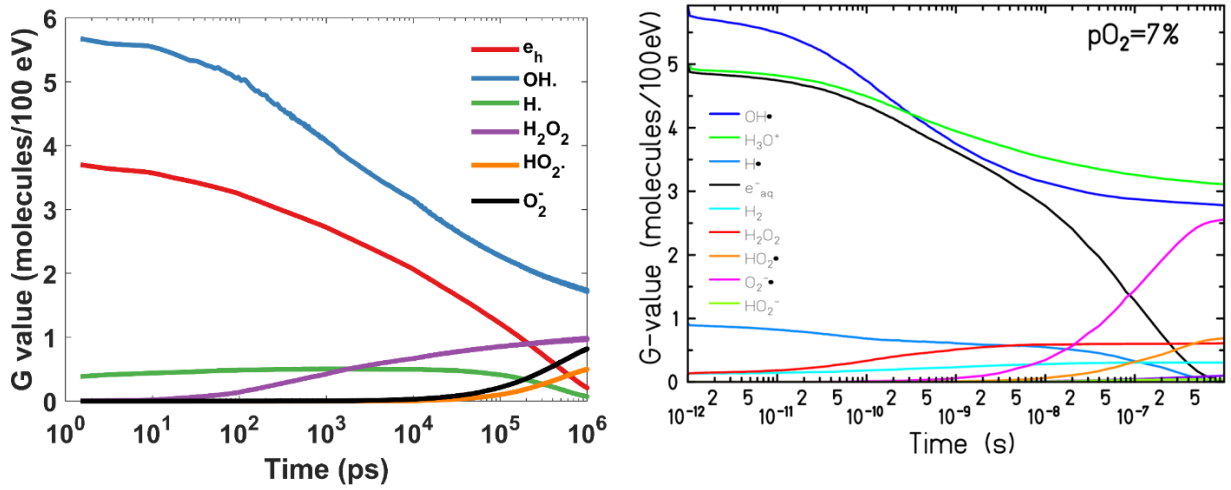

Figure 3.4 Time dependent yield of the chemical species generated by a 90 MeV proton track in an oxygenated target in equilibrium with an atmospheric partial oxygen pressure at the water surface of 7%. Left: from gMicroMC; Right: from work of Boscolo *et. al.* (48).

3.1.2.4 Results at oxygen concentration level at 21%

These results shown in Figure 13 were generated with an oxygen concentration level at 21%. At the beginning of the chemical stage, we can notice that no matter the concentration level of oxygen, initially the only chemical species we have are OH radical, electrons and hydrogen atom. At the time interval of 1 ns, the amount of all six chemical species created also remains relatively the same as for those at the lower oxygen concentration level. It is safe to say that almost no O_2^- and $HO_2^\cdot$ is created at this stage. Another noticeable outcome is at the final of the chemical stage, all of the hydrogen atom and electrons seemed to have been consumed. While the amount of O_2^- and $HO_2^\cdot$ is greater than when compared to the previous concentration levels. The amount of O_2^- and $HO_2^\cdot$ seems to be directly proportional to the number of electrons and hydrogen consumed. Also, the amount of O_2^- produced at this stage is about twice as much as the amount of

$HO_2^{\cdot}$ produced. In the concentration levels of 3%, when O_2^- and $HO_2^{\cdot}$ were produced, it seemed to be relatively around the same amount. Another trend that can be noticed is the oxygen concentration level does not affect the final amount of OH and H_2O_2 produced. As the oxygen concentration level increases, it seems that only hydrogen atom and electrons will be consumed. It also seems that oxygen is needed in order to create O_2^- and $HO_2^{\cdot}$.

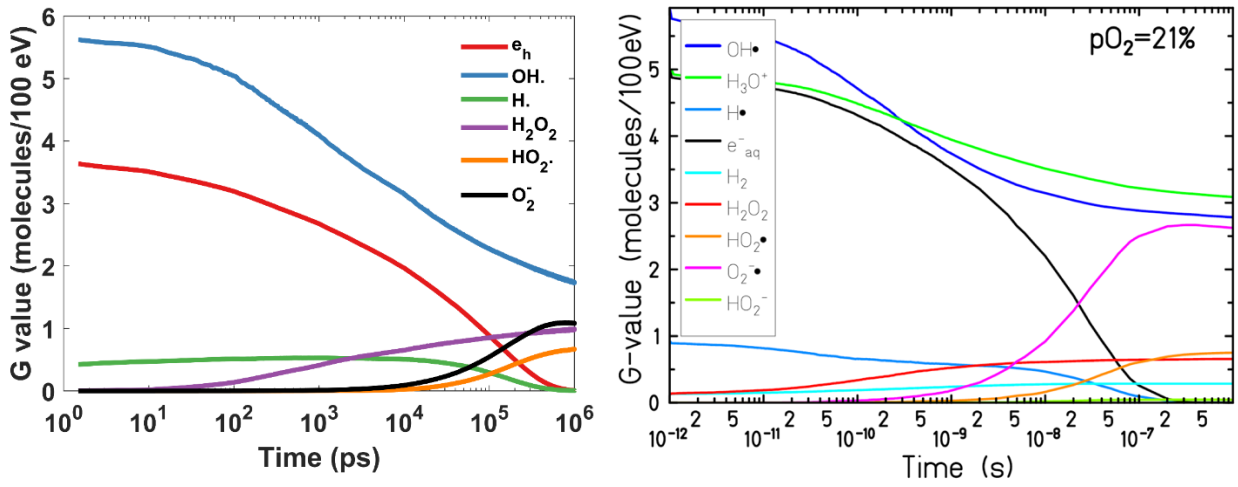

Figure 3.5 Time dependent yield of the chemical species generated by a 90 MeV proton track in an oxygenated target in equilibrium with an atmospheric partial oxygen pressure at the water surface of 21%. Left: from gMicroMC; Right: from work of Boscolo *et. al.* (48).

3.1.2.5 Discussion

In comparison with the work done by Boscolo *et al*., similar to the behavior at 0% oxygen concentration level, at 3%, 7% and 21% levels, the overall time dependence of G-values of different species follow similar increase or decrease trends between gMicroMC and Boscolo's work. Along with the increase of the oxygen concentration level, the G-values of electron radicals decreased more quickly during the chemical stage. On the other hand, the generation of O_2^- and $HO_2^{\cdot}$ were significantly increased with a higher oxygen concentration level. However, there are

also noticeable differences. One is the decreasing rate of electron radicals. When there is no oxygen concentration, the electron radicals were consumed quicker in gMicroMC simulation than in Boscolo's simulation work. However, when the oxygen level increased, the consumption of both free electron radicals and hydrogen atom from Boscolo's work is much faster than that from gMicroMC. From our previous analysis, the main reactor with oxygen molecule is the electron radical and the hydrogen atom. The different behavior of the two species in the two-simulation work can be a reflection of the different treat of the oxygen molecules in the two simulations. This result indicated that along with the oxygen consumption, the oxygen distribution can be non-homogenous, and a changed consumption rate may exist.

3.2 Issues and solutions when using gMicroMC as a fresh user

3.2.1 Geometry setup

To start the simulation, the first critical thing is to correctly setup the geometry for the simulation case. In our simulation study, the initial ROI position along the proton track is not given but indicated by the LET value. However, in gMicroMC, the ROI is set directly relevant to the distance to the source. To solve this issue, we used Geant4 MC simulation tool to transfer the given LET to the position along the proton track, such that we could setup the corresponding position of ROI relative to the proton starting point in gMicroMC.

3.2.2 G value calculation

Second, much effort has been contributing to the correct calculation of G-value. In proton therapy with conventional dose rate, the tracks from different primary proton particles can be taken as independent. Hence, the G-values, representing the number of radicals produced per 100 eV energy deposition, were evaluated per primary particle based. However, the G-value from a single

run can be associated with large fluctuations. To solve this problem, ideally, we could run a primary proton and then recorded its energy deposition E within the ROI and the radicals it produced. We then repeated this process for N times until 2.5 MeV energy deposition inside the ROI was achieved. The energy deposition E_i from primary proton N_i and the corresponding radical list from the physicochemical stage R_i is recorded. The radicals from different primary protons were then separately simulated in the chemical stage. G-values then can be calculated for each primary particle N_i for each radical species as R_{ij} / E_i (in eV) * 100, with j representing the jth radical species. The mean of G-value over the N primary particles then can be calculated as

$$G_j = \sum_{i=1}^{N} \frac{R_{ij}}{E_i\ (in\ eV)} * 100 \Big/ N. \qquad (1)$$

In the current version of gMicroMC, the energy deposition from each primary proton is printed on the running screen but not separately recorded into the file, while the total accumulated energy E_{total} from N simulated primary particles can be obtained. The radical list from each primary is also separately stored and the chemical stage for each radical list is then performed. Hence in gMicroMC, the actual G value is calculated as

$$G_j = \frac{\sum_{i=1}^{N} R_{ij}/N}{E_{total}/N} * 100. \qquad (2)$$

3.2.3 Maximum memory allocation

Another minor problem that would occur was the adjustment of the MAXIMUM allowed particle numbers in each stage computation. Specifically, the maximum number of particles in the physicochemical stage and maximum oxygens and particles in the chemical stage are predefined and the thread parallelization and GPU memory allocation will be automatically performed based on it. To optimize the simulation efficiency, this number is typically set large enough to enable the

simulation of all input particles while not too large to save the memory. Otherwise if the MAXIMUM number is not large enough, some data would be lost or the simulation would just crash if the error kept occurring. Hence, before performing the systematic simulation for each case, a trial run will be needed to determine the optimal maximal numbers for each stage. A critical point is that the radicals produced for each run can be of a fluctuation of 15% if the radical count is not large. The trick is that we always set the MAXIMUM number of 115% of the corresponding number from the trial run.

3.2.4 Discussion

As for the G value computation, the current method available in gMicroMC as shown in Eq. (2) can be taken as equivalent to that stated in Eq. (1) when the simulated particle is large. In the current study, the simulated particle is typically between 150-200, which is large enough to make G values from Eq. (2) within acceptable accuracy level when compared with Eq. (1). Yet, to make it more tolerance to more general cases, a modification of the code to allow the output of the recorded energy for each primary particle may be needed.

The maximum number issue can be tricky, since it can be easily to be forgot to change it for each simulation case or it can be inconvenient for automatically run multiple cases through scripts. In our future work, the number may be dynamically and automatically set according to the simulation results from last step.

CHAPTER 4: CONCLUSION AND FUTURE WORK

Dissolved oxygen molecules are known to play an important role in radiotherapy. For example, tumor cells can be more radio-resistance under hypoxia than normoxia. Macroscopically, this was quantified as the oxygen enhancement ratio (OER). There has been multiple hypothesis proposed to explain these phenomena, including the oxygen mediated chemical track evolution, oxygen fixation effect, etc. In principle, we can perform microscopic Monte Carlo (MC) simulation to quantitively test this hypothesis. Yet, to avoid the extreme high computational resource consuming, in the current CPU-based MC tools, oxygen is either ignored or taken as a continuous radical-scavenging background.

Recently, our research group developed an open-source, GPU-based MC simulation tool, gMicroMC, in which, the oxygen mediated chemical track evolution was modeled in a step-by-step manner. In this project, we applied gMicroMC to study the radical evolution under different oxygen levels for proton induced water radiolysis. Compared to the continuous background method, the oxygen was found consumed slower with gMicroMC. This result indicated that along with the oxygen consumption, the oxygen distribution can be non-homogenous, and a changed consumption rate may exist. We also documented the errors and issues as a fresh user of gMicroMC. In general, gMicroMC is robust to simulate the water radiolysis for different oxygen levels. A further automation for some parameter settings can make it more user-friendly.

In this thesis, we only computed the oxygen effect for low LET region of the proton induced water radiolysis process. To make it more comprehensive, in our future work, we will apply similar simulation for the high LET region, which can be of more interest for the tumor treatment. Furthermore, since radiotherapy with x-ray beams has a much higher OER than proton beam, we

will also examine the oxygen effect with x-ray induced water radiolysis under different energy levels.

REFERENCES

1. Rimpler A, Veit R, Nosske D, Brix G. [Radiation hygiene in medical X-ray imaging, part 1: physical and technical basics]. Radiologe. 2010;50(9):809-20.
2. Seibert JA. X-ray imaging physics for nuclear medicine technologists. Part 1: Basic principles of x-ray production. J Nucl Med Technol. 2004;32(3):139-47.
3. Hayashi M. Bibliography of electron and photon cross sections with atoms and molecules. Published in the 20th century. Methane. National Inst. for Fusion Science; 2004.
4. Wu J, Hei TK. Focus small to find big - the microbeam story. Int J Radiat Biol. 2018;94(8):782-8.
5. Mavragani IV, Nikitaki Z, Kalospyros SA, Georgakilas AG. Ionizing Radiation and Complex DNA Damage: From Prediction to Detection Challenges and Biological Significance. Cancers (Basel). 2019;11(11).
6. Iqbal A, Ullah N, Ur Rahman A. Density-dependent Energy Loss of Protons in Pb and Be Targets and Percent Mass-Stopping Power from Bethe-Bloch Formula and Bichsel-Sternheimer Data Within 1-12 MeV Energy Range: A Comparative Study Based on Bland-Altman Analysis. J Med Imaging Radiat Sci. 2019;50(1):149-56.
7. Lewis GD, Holliday EB, Kocak-Uzel E, Hernandez M, Garden AS, Rosenthal DI, et al. Intensity-modulated proton therapy for nasopharyngeal carcinoma: Decreased radiation dose to normal structures and encouraging clinical outcomes. Head Neck. 2016;38 Suppl 1:E1886-95.
8. Hamada N, Imaoka T, Masunaga S, Ogata T, Okayasu R, Takahashi A, et al. Recent advances in the biology of heavy-ion cancer therapy. J Radiat Res. 2010;51(4):365-83.
9. Olive PL. The role of DNA single- and double-strand breaks in cell killing by ionizing radiation. Radiat Res. 1998;150(5 Suppl):S42-51.
10. Iliakis G, Wang Y, Guan J, Wang H. DNA damage checkpoint control in cells exposed to ionizing radiation. Oncogene. 2003;22(37):5834-47.
11. Bourhis J, Montay-Gruel P, Goncalves Jorge P, Bailat C, Petit B, Ollivier J, et al. Clinical translation of FLASH radiotherapy: Why and how? Radiother Oncol. 2019;139:11-7.
12. Varlotto J, Stevenson MA. Anemia, tumor hypoxemia, and the cancer patient. Int J Radiat Oncol Biol Phys. 2005;63(1):25-36.
13. Barendsen GW. RBE-LET relationships for different types of lethal radiation damage in mammalian cells: comparison with DNA dsb and an interpretation of differences in radiosensitivity. Int J Radiat Biol. 1994;66(5):433-6.
14. Barendsen GW. The relationships between RBE and LET for different types of lethal damage in mammalian cells: biophysical and molecular mechanisms. Radiat Res. 1994;139(3):257-70.

15. Chadwick KH. Understanding radiation biology : from DNA damage to cancer and radiation risk. Boca Raton: CRC Press; 2020. pages cm p.
16. Watson JD, Crick FH. The structure of DNA. Cold Spring Harb Symp Quant Biol. 1953;18:123-31.
17. Dahm R. Friedrich Miescher and the discovery of DNA. Dev Biol. 2005;278(2):274-88.
18. DuPraw EJ. Macromolecular organization of nuclei and chromosomes: a folded fibre model based on whole-mount electron microscopy. Nature. 1965;206(982):338-43.
19. Kavenoff R, Zimm BH. Chromosome-sized DNA molecules from Drosophila. Chromosoma. 1973;41(1):1-27.
20. Müssig D. Re-scanning in scanned ion beam therapy in the presence of organ motion: Technische Universität; 2014.
21. Grimes DR, Partridge M. A mechanistic investigation of the oxygen fixation hypothesis and oxygen enhancement ratio. Biomed Phys Eng Express. 2015;1(4):045209.
22. Boscolo D, Kramer M, Fuss MC, Durante M, Scifoni E. Impact of Target Oxygenation on the Chemical Track Evolution of Ion and Electron Radiation. Int J Mol Sci. 2020;21(2).
23. Cross CE, Halliwell B, Borish ET, Pryor WA, Ames BN, Saul RL, et al. Oxygen radicals and human disease. Ann Intern Med. 1987;107(4):526-45.
24. Sullivan LB, Chandel NS. Mitochondrial reactive oxygen species and cancer. Cancer Metab. 2014;2:17.
25. Incerti S, Ivanchenko A, Karamitros M, Mantero A, Moretto P, Tran HN, et al. Comparison of GEANT4 very low energy cross section models with experimental data in water. Medical Physics. 2010;37(9):4692-708.
26. Danjo A, Nishimura H. Elastic-Scattering of Electrons from H2o Molecule. J Phys Soc Jpn. 1985;54(4):1224-7.
27. Katase A, Ishibashi K, Matsumoto Y, Sakae T, Maezono S, Murakami E, et al. Elastic-Scattering of Electrons by Water-Molecules over the Range 100-1000 Ev. J Phys B-at Mol Opt. 1986;19(17):2715-34.
28. Johnstone WM, Newell WR. Absolute Vibrationally Elastic Cross-Sections for Electrons Scattered from Water-Molecules between 6 Ev and 50 Ev. J Phys B-at Mol Opt. 1991;24(16):3633-43.
29. Shyn TW, Grafe A. Angular-Distribution of Electrons Elastically Scattered from Water-Vapor. Phys Rev A. 1992;46(7):4406-9.
30. Cho H, Park YS, Tanaka H, Buckman SJ. Measurements of elastic electron scattering by water vapour extended to backward angles. J Phys B-at Mol Opt. 2004;37(3):625-34.
31. Sueoka O, Mori S, Katayama Y. Total Cross-Sections for Electrons and Positrons Colliding with H2o Molecules. J Phys B-at Mol Opt. 1986;19(10):L373-L8.
32. Szmytkowski C. Absolute Total Cross-Sections for Electron-Water Vapor Scattering. Chem Phys Lett. 1987;136(3-4):363-7.

33. Zecca A, Karwasz G, Oss S, Grisenti R, Brusa RS. Total Absolute Cross-Sections for Electron-Scattering on H2o at Intermediate Energies. J Phys B-at Mol Opt. 1987;20(4):L133-L6.
34. Armstrong WD. The chemical basis of radiation damage. Postgrad Med. 1958;23(5):499-507.
35. Alizadeh E, Orlando TM, Sanche L. Biomolecular damage induced by ionizing radiation: the direct and indirect effects of low-energy electrons on DNA. Annu Rev Phys Chem. 2015;66:379-98.
36. Frongillo Y, Goulet T, Fraser M, Cobut V, Patau J, Jay-Gerin JJRP, et al. Monte Carlo simulation of fast electron and proton tracks in liquid water-II. Nonhomogeneous chemistry. 1998;51(3):245-54.
37. Halton JH. A retrospective and prospective survey of the Monte Carlo method. J Siam review. 1970;12(1):1-63.
38. Tian Z, Jiang SB, Jia X. Accelerated Monte Carlo simulation on the chemical stage in water radiolysis using GPU. Phys Med Biol. 2017;62(8):3081-96.
39. Emfietzoglou D, Papamichael G, Nikjoo H. Monte Carlo Electron Track Structure Calculations in Liquid Water Using a New Model Dielectric Response Function. Radiat Res. 2017;188(3):355-68.
40. Bernal MA, Bordage M-C, Brown JMC, Davídková M, Delage E, El Bitar Z, et al. Track structure modeling in liquid water: A review of the Geant4-DNA very low energy extension of the Geant4 Monte Carlo simulation toolkit. Physica Medica. 2015;31(8):861–74.
41. Lazarakis P, Bug MU, Gargioni E, Guatelli S, Rabus H, Rosenfeld AB. Comparison of nanodosimetric parameters of track structure calculated by the Monte Carlo codes Geant4-DNA and PTra. Phys Med Biol. 2012;57(5):1231-50.
42. Friedland W, Dingfelder M, Kundrat P, Jacob P. Track structures, DNA targets and radiation effects in the biophysical Monte Carlo simulation code PARTRAC. Mutat Res-Fund Mol M. 2011;711(1-2):28-40.
43. Friedland W, Dingfelder M, Kundrát P, Jacob P. Track structures, DNA targets and radiation effects in the biophysical Monte Carlo simulation code PARTRAC. Mutation Research/Fundamental and Molecular Mechanisms of Mutagenesis. 2011;711(1):28-40.
44. Uehara S, Nikjoo H, Goodhead DT. Comparison and assessment of electron cross sections for Monte Carlo track structure codes. Radiat Res. 1999;152(2):202-13.
45. Nikjoo H, Uehara S. Comparison of various Monte Carlo track structure codes for energetic electrons in gaseous and liquid water. Basic Life Sci. 1994;63:167-84; discussion 84-5.
46. Meylan S, Incerti S, Karamitros M, Tang N, Bueno M, Clairand I, et al. Simulation of early DNA damage after the irradiation of a fibroblast cell nucleus using Geant4-DNA. Scientific Reports. 2017;7:11923.

47. Ramos-Mendez J, Perl J, Schuemann J, McNamara A, Paganetti H, Faddegon B. Monte Carlo simulation of chemistry following radiolysis with TOPAS-nBio. Physics in Medicine & Biology. 2018;63(10):105014.
48. Boscolo D, Krämer M, Fuss MC, Durante M, Scifoni E. Impact of Target Oxygenation on the Chemical Track Evolution of Ion and Electron Radiation. International Journal of Molecular Sciences. 2020;21(2):424.
49. Colliaux A, Gervais B, Rodriguez-Lafrasse C, Beuve M. Simulation of ion-induced water radiolysis in different conditions of oxygenation. Nuclear Instruments and Methods in Physics Research Section B: Beam Interactions with Materials and Atoms. 2015;365:596-605.
50. Tsai M, Tian Z, Qin N, Yan C, Lai Y, Hung S-H, et al. A new open-source GPU-based microscopic Monte Carlo simulation tool for the calculations of DNA damages caused by ionizing radiation --- Part I: Core algorithm and validation. Medical Physics. 2020;47(4):1958-70.
51. Lai Y, Tsai M, Tian Z, Qin N, Yan C, Hung S-H, et al. A new open-source GPU-based microscopic Monte Carlo simulation tool for the calculations of DNA damages caused by ionizing radiation — Part II: sensitivity and uncertainty analysis. Medical Physics. 2020;47(4):1971-82.
52. Santos JP, Parente F, Kim Y-K. Cross sections for K-shell ionization of atoms by electron impact. Journal of Physics B: Atomic, Molecular and Optical Physics. 2003;36:4211-24.
53. Kim Y-K, Santos JP, Parente F. Extension of the binary-encounter-dipole model to relativistic incident electrons. Physical Review A. 2000;62:52710.
54. Dingfelder M, Hantke D, Inokuti M, Paretzke HG. Electron inelastic-scattering cross sections in liquid water. Radiation Physics and Chemistry. 1998;53:1-18.
55. Olivero J, Stagat R, Green A. Electron deposition in water vapor, with atmospheric applications. Journal of Geophysical Research. 1972;77(25):4797-811.
56. Brenner D, Zaider M. A computationally convenient parameterisation of experimental angular distributions of low energy electrons elastically scattered off water vapour. Physics in Medicine & Biology. 1984;29(4):443.
57. Moliere G. Theorie der streuung schneller geladener teilchen ii mehrfach-und vielfachstreuung. Zeitschrift für Naturforschung A. 1948;3(2):78-97.
58. Melton CE. Principles of Mass Spectrometry and Negative Ions: Dekker (Marcel) Inc.,U.S.; 1971.
59. Bordage MC, Bordes J, Edel S, Terrissol M, Franceries X, Bardies M, et al. Implementation of new physics models for low energy electrons in liquid water in Geant4-DNA. Phys Med. 2016;32(12):1833-40.
60. Edel S. Modélisation du transport des photons et des électrons dans l'ADN plasmide: Thèse de Doctorat, Université Paul Sabatier, Toulouse, France; 2006.
61. Jia X, Yan H, Gu X, Jiang SB. Fast Monte Carlo simulation for patient-specific CT/CBCT imaging dose calculation. Physics in Medicine and Biology. 2012;57(3):577-90.

62. Plante I, Cucinotta FA. Ionization and excitation cross sections for the interaction of HZE particles in liquid water and application to Monte Carlo simulation of radiation tracks. New Journal of Physics. 2008;10(12):125020.
63. Kreipl MS, Friedland W, Paretzke HG. Time- and space-resolved Monte Carlo study of water radiolysis for photon, electron and ion irradiation. Radiation and Environmental Biophysics. 2008;48:11.
64. Plante I. A Monte–Carlo step-by-step simulation code of the non-homogeneous chemistry of the radiolysis of water and aqueous solutions. Part I: theoretical framework and implementation. Radiation and Environmental Biophysics. 2011;50:389-403.
65. Tian Z, Jiang SB, Jia X. Accelerated Monte Carlo simulation on the chemical stage in water radiolysis using GPU. Physics in Medicine and Biology. 2017;62:3081-96.
66. Kreth G, Finsterle J, von Hase J, Cremer M, Cremer C. Radial Arrangement of Chromosome Territories in Human Cell Nuclei: A Computer Model Approach Based on Gene Density Indicates a Probabilistic Global Positioning Code. Biophysical Journal. 2004;86(5):2803-12.
67. Wenger RH, Kurtcuoglu V, Scholz CC, Marti HH, Hoogewijs D. Frequently asked questions in hypoxia research. Hypoxia (Auckl). 2015;3:35-43.